Materials Today Communications 53 (2026) 115456

Contents lists available at ScienceDirect

Materials Today Communications

journal homepage: www.elsevier.com/locate/mtcomm

A hidden correlation between triboelectric performance and glass transition temperature in $0.80Na_{0.5}Bi_{0.5}TiO_3$-$0.20BaTiO_3$/PDMS-based nanogenerators

Žygimantas Logminas[a], Darya Meisak[a,*], Līva Ģērmane[b], Artyom Plyushch[a], Martynas Kinka[a], Ugnius Sviackevičius[a], Muhammad Shahzaib Asad[a], Aleksej Zarkov[c], Gytis Sliaužys[d], Rokas Dobužinskas[d], Andris Šutka[b], Jūras Banys[a]

[a] Institute of Applied Electrodynamics and Telecommunications, Faculty of Physics, Vilnius University, Sauletekio al. 3, Vilnius, LT–10257, Vilnius, Lithuania
[b] Institute of Physics and Materials Science, Faculty of Natural Sciences and Technology, Riga Technical University, P. Valdena 3/7, Riga, LV-1048, Riga, Latvia
[c] Institute of Chemistry, Faculty of Chemistry and Geosciences, Vilnius University, Naugarduko g. 24, Vilnius, LT-03225, Vilnius, Lithuania
[d] Institute of Chemical Physics, Faculty of Physics, Vilnius University, Sauletekio al. 3, Vilnius, LT–10257, Vilnius, Lithuania

ARTICLE INFO

Keywords:
PDMS
Sodium bismuth titanate - barium titanate
Triboelectric nanogenerator
Mechanical energy harvesting
IoT
Self-powered electronics

ABSTRACT

Polydimethylsiloxane (PDMS)-based triboelectric nanogenerators (TENGs) embedded with 14 vol.% $0.80Na_{0.5}Bi_{0.5}TiO_3$-$0.20BaTiO_3$ (NBT-20BT) particles of different sizes were prepared, and their morphology, temperature and frequency dielectric properties, as well as triboelectric output performance, were studied. A series of powders prepared with progressively longer milling durations showed that the particles became finer and their size distribution became narrower, as indicated by the Weibull distribution statistical analysis. The NBT-20BT/PDMS composite films exhibit a low-temperature dynamic glass transition anomaly dependent on NBT-20BT particle size. Due to strong interaction between PDMS and NBT-20BT, the glass transition temperature shifts to higher values than in pure PDMS. The triboelectric output performance of the NBT-20BT/PDMS-based TENGs, tested against an Al foil in a vertical contact-separation mode under a pressing force of 10 N, exhibited a non-monotonic behavior. For the most efficient sample, the triboelectric parameters reached 6.06 μ A, 9.78 nC/cm^2, and 6.23 μW/cm^2 for the short-circuit current, charge density, and output power density, respectively. The observed maximum in the triboelectric properties across the series is explained by the agglomeration of the corresponding powder within the PDMS, as revealed by scanning electron microscopy. An important correlation for the NBT-20BT/PDMS composite films was observed: the TENG output performance depends on the glass transition temperature in a near-linear manner.

1. Introduction

The growing requirement for electronics motivates the search for clean and portable energy sources. Such sources include, but are not limited to, wind, solar, chemical, and thermal energy, which can be collected and exploited. However, current technologies still fail to achieve the required levels of efficiency. Therefore, it is necessary to develop new energy harvesters to solve the power source issues of future functional electronics. Alongside energy-consuming applications, a solution for low-power distributed autonomous microelectronic devices and self-powered sensors is needed.

In the last several years, a new type of energy harvesting technology named as triboelectric nanogenerator (TENG) has emerged to harness energy from ambient mechanical motions. The main working principle is related to the coupling of the effects of contact electrification and electrostatic induction. This implies that two distinct materials are brought into contact and then separated. During contact electrification, charge moves by electron, ion, or even mass transfer [1]. As a result, a pair of materials reveals the potential difference, the direction and value of which depend on the materials involved. Although TENGs were invented relatively recently, in 2012 [2], they have already found a lot of potential applications in practice, primarily in micro/nano-energy harvesting [3,4], sensors [5–7], blue energy harvesting [8–10], and biomechanical harvesting and monitoring [11,12].

As mentioned above, the efficiency of the TENG mainly depends on the materials in contact. For single-phase materials, the situation is well studied and systematized into triboelectric series [13]. As for

* Corresponding author.
Email address: darya.meisak@ff.vu.lt (D. Meisak).

https://doi.org/10.1016/j.mtcomm.2026.115456
Received 13 February 2026; Received in revised form 3 April 2026; Accepted 26 May 2026
Available online 27 May 2026

more complex systems, such as basic two-phase bulk composites, the final properties are less predictable. Focusing on polymer-based TENGs, a significant research has been devoted to improving their triboelectric output performance by incorporating various fillers. A wide range of polymers is used in TENGs [14,15], and their selection depends on device design, constituent materials, and application requirements. Among them, polydimethylsiloxane (PDMS) is especially attractive due to its high flexibility, strong triboelectric negative tendency, and low cost. The list of possible candidates for reinforcing fillers is not limited to ferroelectrics and related materials [16–18]. Hexagonal boron nitride [19], MXenes [20], calcium copper titanate [21], cobalt/nickel ferrite [22], and SiO_2-based particles [23] are used as fillers. Basically, any type of inorganic filler will do the job. In the nanoparticle-polymer composite, an interface forms around the particles, leading to the accumulation of mechanical stress, which in turn triggers charge transfer [14,24]. Sodium bismuth titanate - barium titanate ($0.80Na_{0.5}Bi_{0.5}TiO_3$-$0.20BaTiO_3$ or NBT-20BT) is a novel lead-free ferroelectric solid solution system offering advanced piezoelectric properties [25] and the possibility to modify NBT-xBT host with a wide range of different inclusions [26,27]. However, it has never been investigated as a functional filler in PDMS-based TENGs.

In an effort to improve the performance of polymer-based TENGs, researchers often resort to a simple approach of adjusting and optimizing the filler content. However, the TENG output is also influenced by morphology (e.g., surface roughness [28], stickiness, etc.) and other microscopic factors, such as the filler particle size, arrangement, and distribution. These aspects have received comparatively little attention, with only a limited number of studies addressing them. Meng et al. [29] demonstrated that the TENG and PENG (piezoelectric nanogenerator) performance of PDMS composites loaded with nano-sized (30 nm) barium titanate (BT) is substantially higher compared to those filled with BT microflakes (5–25 μm and 25–60 μm). Although the work demonstrates a clear advantage of using nano-sized particle fillers, the authors primarily investigate the dependence on filler concentration.

In this work, the NBT-20BT solid solution particles were examined as a filler for the PDMS-based TENGs for the first time. Triboelectric output performance, as well as temperature- and frequency-dependent dielectric properties of NBT-20BT/PDMS-based TENGs are analyzed and discussed. The main aim is to study the effect of filler particle morphology (size and distribution in the polymer) on TENG output characteristics, as well as to identify any correlation between dielectric and triboelectric properties. These findings highlight filler morphology as an important output-determining parameter in triboelectric nanogenerators and introduce NBT-20BT/PDMS composites as a promising material for energy harvesting applications.

2. Materials and methods

2.1. $0.80Na_{0.5}Bi_{0.5}TiO_3$-$0.20BaTiO_3$ powders synthesis

For the synthesis of NBT-20BT powders, commercially available titanium dioxide TiO_2 (2320033, 99.8 %), sodium carbonate Na_2CO_3 (223530, ≥ 99.5 %), bismuth oxide Bi_2O_3 (223891, 99.9 %), and barium carbonate $BaCO_3$ (237108, ≥ 99 %) powders were purchased from Sigma-Aldrich. The NBT-20BT was prepared *via* conventional solid-state reaction method [30,31]. The titanium dioxide, sodium carbonate, bismuth oxide, and barium carbonate powders were mixed in appropriate proportions and wet-ground in isopropyl alcohol for 24 h at 150 rpm. For this, a Planetary mono mill PULVERISETTE 6 (Fritsch, Germany) with a grinding pot and 12 mm zirconium oxide balls was used. After milling, the obtained mixture was calcined for 4 h at 900° C. As received, NBT-20BT powder is used as the reference and labeled 1-NBT-BT. To reduce the mean particle size of the 1-NBT-BT powder, the planetary ball milling method was applied. The grinding conditions were as follows: the rotation speed was set to 150 rpm, while the milling durations and the corresponding NBT-20BT powder labels are summarized in Table 1.

Table 1
Labeling of the NBT-20BT powder series versus applied milling time.

Powder labeling	1-NBT-BT	2-NBT-BT	3-NBT-BT	4-NBT-BT	5-NBT-BT
Milling time, h	0	24	72	152	272

2.2. NBT-20BT/PDMS composite films preparation

For the composite film preparation, polydimethylsiloxane (PDMS), Sylgard 184 silicone elastomer, was received from Dow Corning (Midland, MI, USA) as a two-part material consisting of a base and a curing agent. An indium tin oxide-coated polyethylene terephthalate (ITO-PET) film, used as a substrate, was also provided by Sigma-Aldrich.

A simple dispersion method based on the approach described in Meisak et al. [32] was used to prepare composites. A set of five PDMS-based compositions (see Table 1) was fabricated following the protocol described below.

Initially, the appropriate amount of NBT-20BT particles was dispersed in isopropyl alcohol (IPA) using an ultrasonic bath (EMAG EMMI-12HC, 300 W) for 1.5 hours. Subsequently, the required amount of uncured PDMS was added to the NBT-20BT/IPA solution, and the resulting mixture was sonicated for an additional 3 hours. To evaporate the IPA, the NBT-20BT/IPA/PDMS suspension was placed on a hot plate magnetic stirrer at 80° *C* and left for several hours. For the curing stage, a curing agent in a 1:10 ratio to PDMS was introduced into the NBT-20BT/PDMS mixture, followed by gentle manual stirring for 10 minutes. The resulting NBT-20BT/PDMS/hardener slurry was then ready for further casting manipulations and final curing. The mixture was deposited onto an ITO-PET substrate via spin coating at 800 rpm for 120 s using a Polos Spin 150i Spin Coater. Finally, the composite films were thermally cured at 110° *C* for 3 hours. Figure S1(a,b) in Supporting Information presents real images of the empty ITO-PET substrate used and the final NBT-20BT/PDMS composite film, respectively. The blue part is a protective film for the electrically conductive ITO surface, which functions as the bottom contact in triboelectric measurements. As a result, all prepared composite films, regardless of composition, including pure PDMS, exhibited identical geometry—about 0.1 mm in thickness and a 2.5 × 2.5 cm^2 (6.25 cm^2) active area defined by the substrate dimensions. The NBT-20BT content in each PDMS-based composite film was fixed at 14 vol.%.

2.3. Characterization methods

X-ray diffraction (XRD) analysis was carried out using a Rigaku SmartLab SE diffractometer equipped with a standard goniometer and a Cu K_α radiation source (λ = 1.54186 Å), operated at 40 kV and 50 mA. The scan was performed in the $\theta/2\theta$ mode over a range from 5° to 90°, with a step size of 0.01° and a scan speed of 2°/min. The incident slit was set to 2/3°, and 2.5° Soller slits were used on both the incident and receiving sides. A length-limiting slit of 10 mm was applied, and the receiving slit boxes were open. No monochromator or detector slit was used, and the detector was a D/teX Ultra 250. A K_β filter was employed to suppress unwanted radiation. The optics configuration followed a BB (Bragg-Brentano) geometry. Whole Powder Pattern Fitting (WPPF) analysis was conducted using SmartLab Studio II software, using reference patterns from the Crystallography Open Database (COD).

The structural and morphological properties of the powders and composite films were studied by scanning electron microscopy (SEM) using a FlexSEM 1000 II microscope.

The complex dielectric permittivity of the composite films was measured in the 20 Hz–1 MHz frequency range using an HP4284A LCR meter. For measurements below room temperature, a liquid nitrogen-based cooling system was applied. The rate of the temperature change was not more than 1.5 K/min. For dielectric tests, the bottom contact was ITO, while the top contact was deposited silver.

2.4. Triboelectric measurements

For triboelectric measurements, the spin-coated NBT-20BT/PDMS composite film (see Supporting Information, Figure S1(b)) was attached to a 3D-printed holder of a similar shape (Figure S1(c)) to avoid bending of the substrate. The resulting structure, ready for triboelectric measurements, is shown in Figure S1(d). The blue protective film must be removed before measurements.

The NBT-20BT/PDMS-based TENG devices were measured in contact-separation TENG mode (see Fig. 6a)) under controlled conditions—a separation distance of 5 mm, a pressing force of 10 N, and a frequency of 1 Hz. Triboelectric measurements were performed under a "sawtooth"-profile contact-separation cycle, in which slow approaching was followed by fast separating. In TENG, PDMS film and aluminum (Al) foil functioned as the friction layers. The Al foil served as both the top contact and bottom electrode, whereas ITO served as the bottom electrode. The surface area of the Al foil was 2 cm^2. To ensure repeatability, the contact-separation motion was performed using an Instron E1000 material testing machine. The generated output signals were measured using a Keithley 6514 electrometer connected to a PicoScope 5444B oscilloscope. The measured triboelectric output parameters included open-circuit voltage (V_{OC}), short-circuit current (I_{SC}), as well as voltage (V_L) and current (I_L) across an external load resistance. To measure the respective parameters, the corresponding electrical circuits (see Figs. 6(b, c) and 8(a, b), insets) were connected to the TENG. Load resistances ranged from 10 kΩ to 100 GΩ.

3. Results and discussion

3.1. Characterization of NBT-20BT powders and NBT-20BT/PDMS composite films

The X-ray pattern of the reference 1-NBT-BT powder is presented in Fig. 1(a). The spectrum of the measured sample shows paired peaks, indicating two phases: cubic Pm-3m $BaTiO_3$, 18.7 wt.%, a = 4.0038 Å, COD #1507757 and tetragonal P4bm $Na_{0.5}Bi_{0.5}TiO_3$, 81.3 wt.% a = b = 5.5164, c = 3.9011 Å, COD #2103296 [33]. Both phases are not typical at room temperature: BT is recognized to have a tetragonal structure, while NBT possesses a more complex crystalline structure that remains a topic of debate [34]. It is often described as having either rhombohedral [35] or monoclinic symmetry [36]. The presence of these atypical space groups in both phases suggests partial interdiffusion between the phases and the partial formation of a solid solution. This idea is supported by scanning electron microscopy. The SEM images of the 1-NBT-BT powder with EDX mapping of Bi and Ba are presented in Fig. 1(b–d). Brighter spots in EDX correspond to the presence of the selected element. The distribution of Bi is similar to that of Ba, indicating the absence of single-phase $Na_{0.5}Bi_{0.5}TiO_3$ or $BaTiO_3$ grains.

For the estimation of the mean particle size of NBT-20BT powders, scanning electron microscopy (SEM) was used. Fig. 2(a–c) shows SEM images of the 1-NBT-BT, 3-NBT-BT, and 5-NBT-BT, while those of the 2-NBT-BT and 4-NBT-BT powders are provided in the Supporting Information (Figure S2(a,b)). Fig. 2(a) presents the as-calcined 1-NBT-BT powder, consisting of highly agglomerated particles. It is expected to exhibit the largest mean particle size, followed by a monotonic decrease from sample 1 to 5. For an accurate quantitative determination of particle sizes in the powders, a statistical analysis of SEM images was performed. A sufficiently large number of particle diameter measurements (more than 200) was collected for each powder sample. The particle sizes were demonstrated to obey a Weibull distribution function $F = 1 - e^{-(x/\lambda)^k}$, where λ is the scale parameter and k, the Weibull modulus, is the shape parameter. The Weibull distribution is commonly used to describe powders [37,38]. A typical distribution of particle sizes fitted with a Weibull cumulative distribution function (CDF) is presented in the Supporting Information (Figure S2(c)), while Fig. 2(d) and Figure S2(d) show the evolution of the scale parameter λ and the Weibull modulus k for all NBT-20BT powders, respectively. As the ball-milling time increases, both k and λ decrease. This indicates that the particles are becoming finer (λ drops from 243 to 171 nm) and their size distribution is narrower. The Weibull modulus k is related to the mean particle size as $\langle d \rangle = \lambda\Gamma(1 + 1/k)$, where Γ is Euler's gamma function, which is close

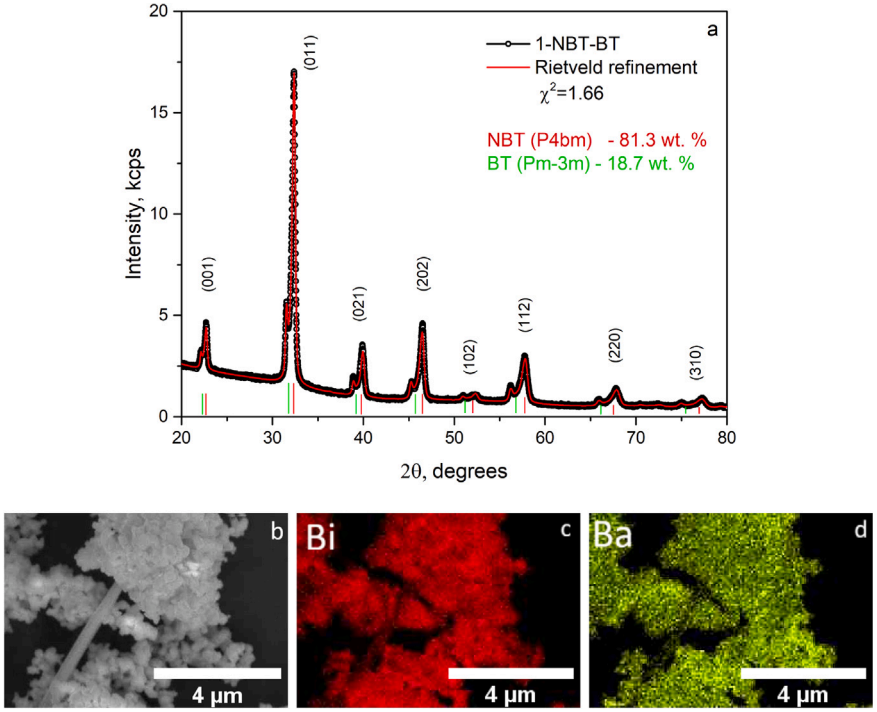

Fig. 1. Characterization of $0.80Na_{0.5}Bi_{0.5}TiO_3$-$0.20BaTiO_3$ powder calcined at 900° C (1-NBT-BT): (a) X-ray diffraction pattern; (b) scanning electron microscopy image; elemental distribution maps of (c) Bi and (d) Ba.

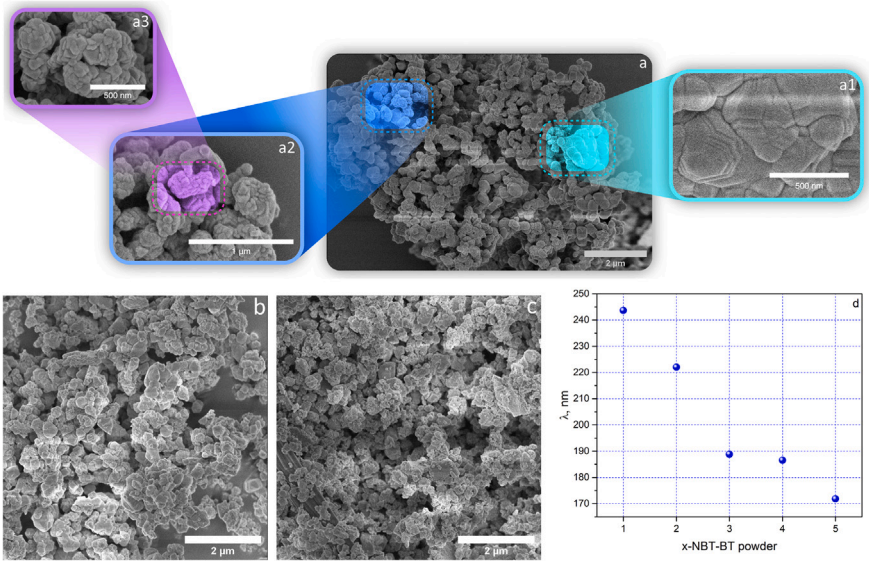

Fig. 2. Scanning electron microscopy images of (a) 1-NBT-BT; (b) 3-NBT-BT; and (c) 5-NBT-BT powders. (d) The scale parameter λ of the Weibull distribution for all NBT-20BT powders studied.

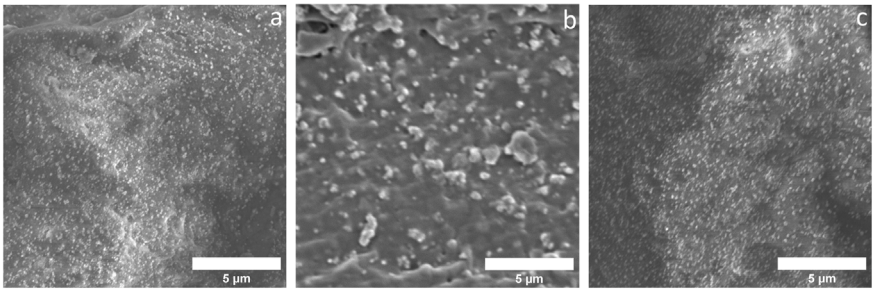

Fig. 3. Scanning electron microscopy images of (a) 1-NBT-BT/PDMS; (b) 3-NBT-BT/PDMS; and (c) 5-NBT-BT/PDMS composite films.

to 1. In addition to the reduction in particle size, milling also gradually decreases the amount of particle agglomeration.

A SEM image of the 1-NBT-BT/PDMS, 3-NBT-BT/PDMS, and 5-NBT-BT/PDMS samples is presented in Fig. 3(a–c). Bright regions correspond to NBT-20BT particles, while the darker areas in between correspond to PDMS. The results are somewhat contradictory. Both the 1-NBT-BT/PDMS and 5-NBT-BT/PDMS samples exhibit a homogeneous particle distribution. The agglomerates of 1-NBT-BT/PDMS sample are of similar size compared to powder, and no agglomerates are detected for 5-NBT-BT/PDMS. In contrast, the 3-NBT-BT/PDMS sample demonstrates agglomerated particles, similar to those found in the SEM of powders (see Fig. 2), together with individual crystallites, although the preparation procedure was exactly the same for all films. The phenomenon of re-agglomeration of ferroelectric nanoparticles in polymers was observed previously. Several possible reasons for such behavior can be highlighted. In general, reasons can be divided into polymer-particle and particle-particle interactions. Researchers attribute this to results of capillary forces during the curing step [39,40]. Boorman et al. conclude that changes to the $BaTiO_3$ structure due to ball milling and a subsequent shift of the isoelectric pH are likely causes of the re-agglomeration of particles in polystyrene-based composites [41]. Another possible reason is the interparticle attractive forces. The ball milling breaks down particles that form the activated newly created surfaces that act as attracting centers [42,43]. Another possible reason is the preparation protocol. Ultrasonic treatment effectively reduces the size of agglomerates, but the dynamics of the process, and the impact of influencing factors are still under study [44].

3.2. Dielectric properties of NBT-20BT/PDMS composite films

The temperature dependencies of the real (ε') and imaginary (ε") parts of the complex dielectric permittivity at a frequency of 100 kHz for all NBT-20BT/PDMS composite films are presented in Fig. 4(a, b). The frequency spectra of ε' at room temperature for all NBT-20BT/PDMS samples are presented in the Supporting Information (Figure S3).

The addition of NBT-20BT to PDMS leads to an increase in ε' from about 4 (for pure PDMS) [45] to 7.5-9 (depending on the specific composition) at room temperature; moreover, ε' is nearly frequency-independent within the investigated range. The ε' demonstrates an anomaly close to 170 K accompanied by a sharp peak in the ε" part. This behavior is attributed to the α-relaxation glass transition of PDMS [46]. The glass transition temperature depends on several factors: molecular weight of PDMS, inclusions, preparation protocol, and conditions [46–48]. To describe in detail the impact of NBT-BT particles of different sizes on the glass transition of PDMS, the temperature dependencies of ε', ε" for each composite were studied at different frequencies. Fig. 4(c, d) shows the data for the 4-NBT-BT/PDMS composite film as an example. Since the other samples exhibit similar behavior, their dependencies of ε' and ε" are not included here. The real part of ε gradually decreases with frequency in the range of 150–200 K (see Fig. 4c). The sharp peak in dielectric losses between 160–170 K is frequency-dependent and shifts toward higher temperatures as the frequency increases (Fig. 4d). Above 200 K, no frequency dispersion is observed in either ε' or ε".

The position of the maximum in the dielectric losses (at fixed frequency) depends on the size of NBT-20BT particles in a non-monotonic

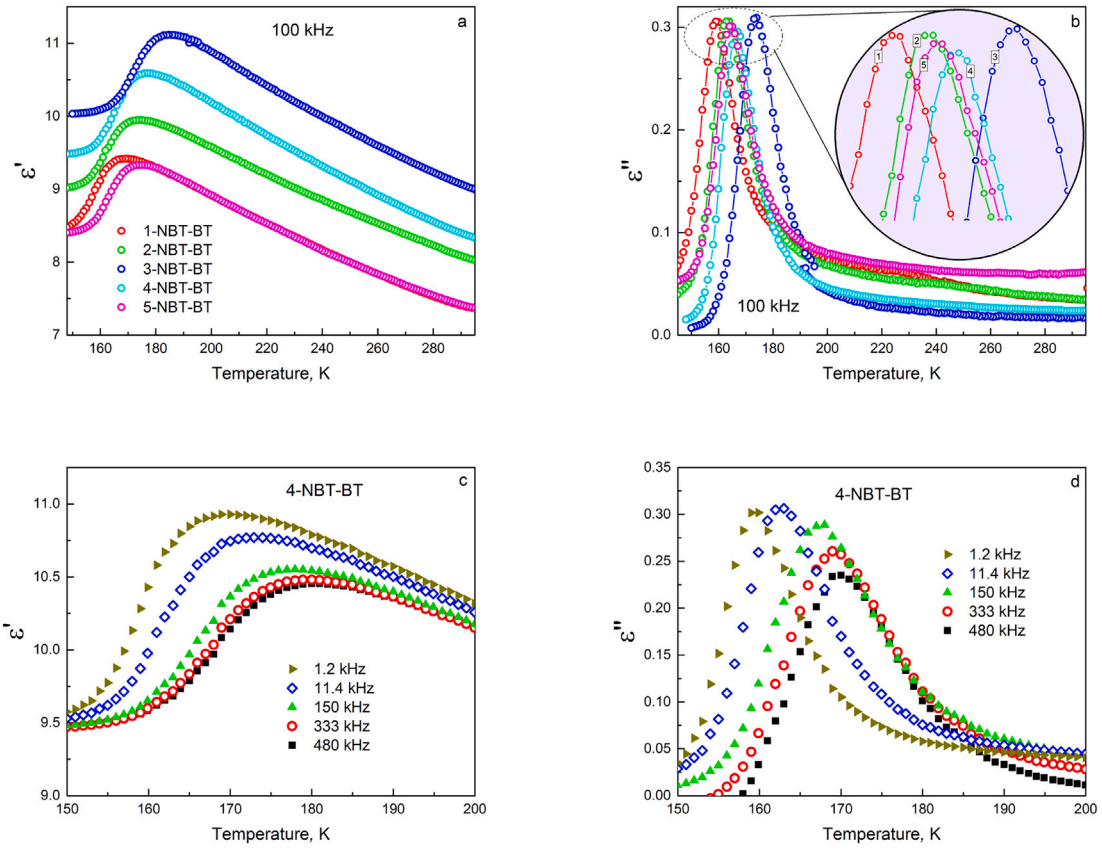

Fig. 4. Temperature dependencies of (a) the real and (b) the imaginary parts of the dielectric permittivity at 100 kHz frequency for NBT-20BT/PDMS composite films. Inset: Enlargement of the dielectric loss peak region. Temperature dependencies of (c) the real part of the dielectric permittivity and (d) dielectric losses at different frequencies for 4-NBT-BT/PDMS composite film.

manner (see Fig. 4b (inset)). Namely, with decreasing NBT-20BT particle size, the maximum of ε" shifts toward higher temperatures. For the 3-NBT-BT/PDMS sample, this peak is observed at the highest temperature value (the rightmost curve). From the 4-NBT-BT/PDMS sample, the peak shifts in the opposite direction.

Knowing the glass transition temperature enables the characterization of the chemical bonding between the PDMS matrix and the NBT-20BT inclusions. To determine the glass transition temperature, the position of the dielectric loss peaks as a function of frequency (see Fig. 4(d)) for all NBT-20BT/PDMS composite films under study was analyzed using the Vogel-Fulcher law (see Fig. 5):

$$\nu = \nu_0 \exp\left(\frac{-E_{\mathrm{VF}}}{k_B(T_{\max} - T_g)}\right) \quad (1)$$

where ν is the frequency, ν_0 is the frequency when T_{max} is infinite, E_{VF} is the Vogel-Fulcher activation energy, k_B is the Boltzmann constant, T_g is the glass transition temperature of the composite, and T_{max} is the temperature of maximum in ε". The solid lines in Fig. 5 correspond to the best fits; their parameters are summarized in Table 2. Table 2 shows a strong correlation between the glass transition temperature and the Vogel–Fulcher activation energy with the size of NBT-20BT particles. Both T_g and E_{VF} initially increase with milling time for 1-NBT-BT and 2-NBT-BT samples, reach a maximum for 3-NBT-BT samples, and decrease for the 4-NBT-BT and 5-NBT-BT samples.

The glass transition in polymers strongly depends on the mobility of the polymer chains [46], which decreases with cooling. As such, an increase in glass transition temperature is indicative of a reduction in mobility due to interaction between fillers and polymers. Łapińska et al. [49] and Plyushch et al. [45] have studied this phenomenon. As shown

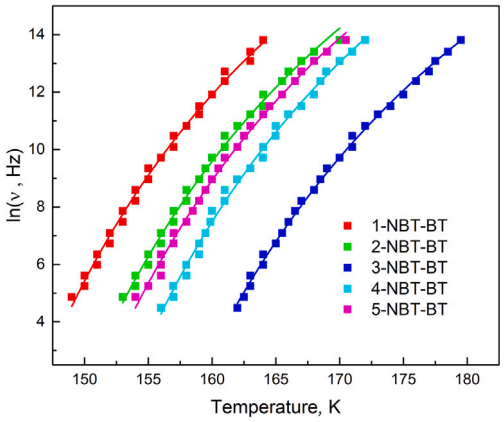

Fig. 5. Frequency versus temperature at maximum dielectric loss for NBT-20BT/PDMS composite films. Solid lines are best fits to the Vogel-Fulcher law (Eq. (1)).

in Table 2, the glass transition temperature of pure PDMS is lower than that of all other samples of NBT-20BT/PDMS. This indicates that the NBT-20BT filler (regardless of size) interacts strongly with the PDMS chains. The interaction mentioned is strongest in the 3-NBT-BT/PDMS composite film, which exhibits the highest glass transition temperature.

3.3. Triboelectric output performance of NBT-20BT/PDMS-based TENGs

As the TENG operates (see Fig. 6a), periodic contact-separation movements induce surface charge transfer in the contact area and charge

Table 2
Glass transition temperatures and Vogel-Fulcher activation energies of NBT-20BT/PDMS composite films (Here, * denotes data for pure PDMS taken from ref. [32]).

Sample	E_{VF}, eV	T_g, K	ν_0, THz
* PDMS	–	* 117.4	–
1-NBT-BT	0.076	117.8 ± 0.5	179.3
2-NBT-BT	0.080	119.9 ± 0.6	179.3
3-NBT-BT	0.088	125.6 ± 0.4	179.3
4-NBT-BT	0.078	124.4 ± 0.6	179.3
5-NBT-BT	0.079	121.7 ± 0.5	179.3

accumulation on the triboelectric layers due to the triboelectrification phenomenon. Additionally, due to electrostatic induction, an electric potential difference is established between the two electrodes. In order for this mechanism to function effectively, the triboelectric layers must exhibit opposing tribo-polarities. In the present TENG configuration, the PDMS-based film serves as the negative tribo-layer, while the Al foil plays a dual role as both the top electrode and the positive tribo-layer. Al foil was chosen as the opposite contact surface to ensure that the tribo-materials are located on different sides of the triboelectric series [50]. If the two electrodes are connected through a load or short-circuited, the induced potential difference drives electrons to flow back and forth between the electrodes, resulting in an alternating current in the external circuit.

To illustrate the functional mechanism of NBT-20BT/PDMS-based TENG against aluminum, the electric output of the open-circuit voltage (V_{OC}) and the short-circuit current (I_{SC}) for one working cycle at 1 Hz (one contact and one separation) is enlarged in Fig. 6(b and c), respectively. The V_{OC} voltage switches between two potential levels: one corresponds to the contact position (lower level), while the other corresponds to the separation or original position (higher level). Notably, the potential difference arises at the moments of approaching and separating. As the TENG is separated, V_{OC} increases, reaching its maximum when the Al foil fully returns to its original position. If the two friction layers approach immediately—that is, they come into contact again—V_{OC} drops from its higher level to the lower level as full contact between the layers is re-established. When the two electrodes are short-circuited, any induced potential difference drives electron flow from the top electrode to the bottom electrode and vice versa. During the separation step, the electron flow results in an instantaneous positive current, whereas during the approaching step, it produces a negative current. The difference in the signal shapes for the positive and negative directions is attributed to the character of the approaching and separating motions. A short, broad negative current pulse corresponds to slow

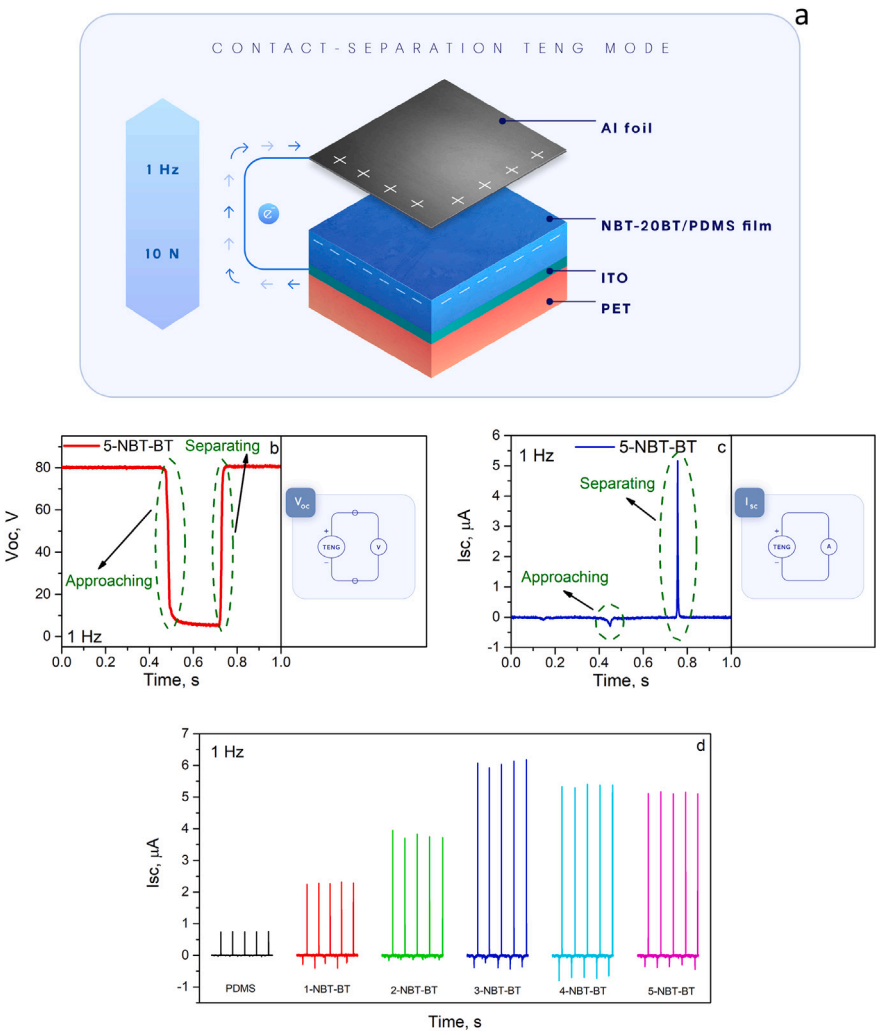

Fig. 6. (a) Schematic illustration presenting the NBT-20BT/PDMS-based TENG device in a contact-separation configuration. Enlargement of one cycle open-circuit voltage V_{OC} (b) and short-circuit current I_{SC} (c) pulses for the 5-NBT-BT/PDMS sample as an example. (d) short-circuit current (I_{SC}) signals generated from NBT-20BT/PDMS-based TENGs (all compositions) under a periodic compressive force of 10 N at a contact–separation frequency of 1 Hz.

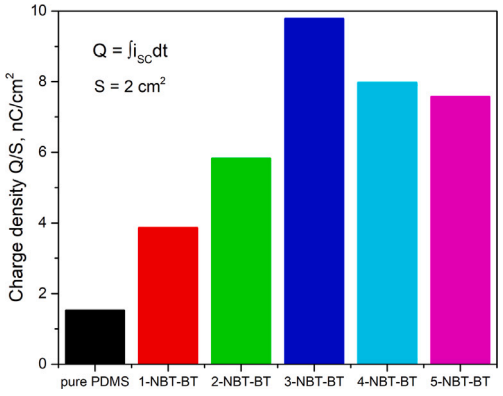

Fig. 7. Surface charge density of NBT-20BT/PDMS-based composite samples in contact-separation (1 Hz, 10 N) against an Al electrode, calculated from the positive peaks of measured I_{SC} signals corresponding to the separation stage.

approaching, while a long, narrow positive pulse corresponds to fast separating. Importantly, the total charge transferred in both directions remains equal within a single cycle (as illustrated below for the studied system).

Fig. 6(d) shows short-circuit current signals I_{SC} (5 pulses) generated from NBT-20BT/PDMS-based TENGs (all compositions/particle sizes) under a periodic compressive force of 10 N at a contact–separation frequency of 1 Hz. Pure PDMS exhibits the smallest signal I_{SC}, with a peak-to-peak value of 0.78 μ A. Incorporation of NBT-20BT particles, regardless of their size, leads to an increase in I_{SC}. The observed increases in short-circuit current and surface charge density (presented below) are typical for similar systems [51–53], and are attributed to enhanced polarization induced by the inclusion of high-permittivity particles in the negative tribo-material. Furthermore, as the particle size of NBT-20BT decreases (from No. 1 to 5), the I_{SC} exhibits a non-monotonic behavior: it initially increases and reaches its maximum at the 3-NBT-BT/PDMS sample (peak-to-peak value of 6.36 μ A), followed by a subsequent decrease.

The surface charge (Q) transferred in opposite directions during the approach and separation can be quantitatively estimated from short-circuit current measurements. The charge Q can be calculated by integrating the measured peaks in the signal I_{SC} over time (see Figs. 6(c, d)), as $Q = \int i_{SC}\, dt$. Both peaks (positive and negative, corresponding to the separation and approaching stages, respectively) were integrated to obtain the transferred Q values in both directions. The surface charge density is calculated as Q/S, where S represents the friction contact area, which is fixed at 2 cm^2. The calculated values from the positive peaks of I_{SC} surface charge densities for NBT-20BT/PDMS-based composite samples in contact-separation mode (1 Hz, 10 N) against an Al electrode are presented in Fig. 7, while Q/S values calculated from the negative peaks are provided in the Supporting Information (Figure S4). In addition, both $\pm Q/S$ values are presented in Table S1 (Supporting Information). These results indicate that the total charge transferred in both directions remains nearly equal within one cycle (one approaching and one separating stage). Furthermore, the trend in surface charge density behavior correlates well with the short-circuit current response across different samples (see Fig. 6(d)); in particular, as the particle size of NBT-20BT decreases, Q/S increases and reaches maximum value of 9.78 nC/cm^2 (-9.42 nC/cm^2) for 3-NBT-BT/PDMS, followed by a subsequent decrease.

To further evaluate the effective output performance of the NBT-20BT/PDMS-based TENGs, external resistors (ranging from 10 kΩ to 100 GΩ) were connected as load elements. Fig. 8(a, b) presents the root mean square (RMS) voltage and current values, as well as the output power density, across various external load resistances for the 4-NBT-BT/PDMS-based TENG as an example. RMS values were extracted for each specific load resistance from the corresponding continuous-time signals recorded over a 20 s interval.

The power density was calculated according to the following procedure [54]. First, the instantaneous power was calculated as $P(t) = V^2/R$, where V is the measured voltage data and R is the corresponding load resistance. The instantaneous power was then plotted as a function of time. Next, by integrating the area under the power peak, the energy E generated during the releasing step was determined. The peak duration Δt was also extracted from the plot and used to compute the average power during the releasing step using the formula $P = E/\Delta t$. Finally, the power density was calculated by dividing the average power by the friction contact area (2 cm^2).

The behavior shown in Fig. 8(a, b) is typical [55,56]. Namely, as the load resistance increases, the current decreases, while the voltage increases. Moreover, at low (<10^6 Ω) and high (>10^9 Ω) resistance values, the voltage and current are weakly dependent on R, while in the intermediate range, strong dispersion is observed. The output power density (Fig. 8a, green curve) exhibits a maximum at a certain load resistance.

To evaluate the maximum output power density (P_{max}) and the corresponding load resistance (R_{max}) for all NBT-20BT/PDMS-based TENGs under study, the output P was plotted as a function of external resistance R in a log-log scale (see Fig. 9). The resulting $log P$ $vs.$ $log R$ curves were fitted using a parabolic function (solid lines in Fig. 9). Based on the fitting parameters, the maximum was determined analytically by locating the extremum via the first derivative condition. The obtained values of P_{max} and their associated R_{max} for all samples are summarized in Table 3.

A trend in the maximum output power density was observed, similar to that of I_{SC} and Q/S. The P_{max} first increases, reaching its peak

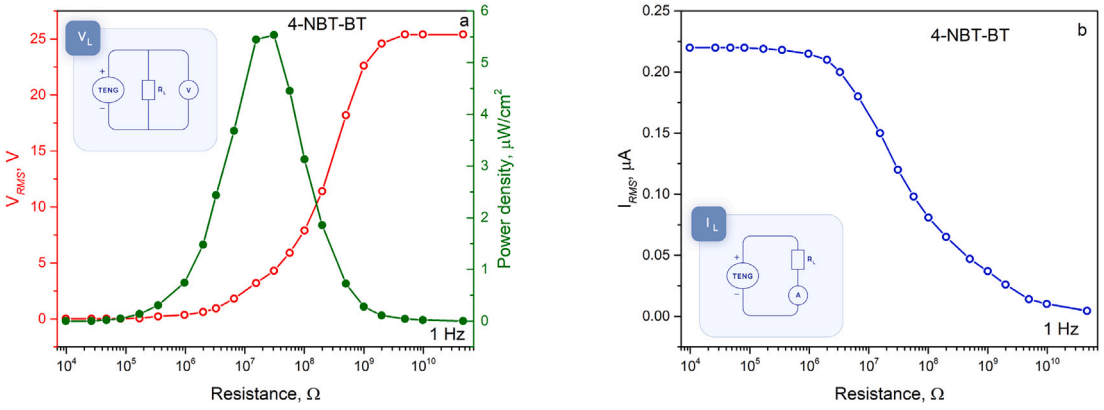

Fig. 8. Dependence of output (a) power density, voltage and (b) current on the external load resistance for the 4-NBT-BT/PDMS-based TENG as an example.

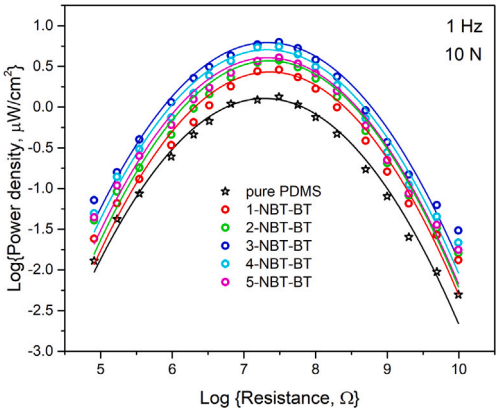

Fig. 9. Dependence of the output power density on external load resistance (log–log scale) at a compressive force of 10 N and a frequency of 1 Hz for NBT-20BT/PDMS-based TENGs. The solid lines represent parabolic fits. The maximum output power values and corresponding load resistances are listed in Table 3.

Table 3
Maximum output power values and corresponding load resistances for NBT-20BT/PDMS-based TENGs, obtained from parabolic fits.

Sample	R_{max}, MΩ	P_{max}, μW/cm^2
pure PDMS	19.39	1.28
1-NBT-BT/PDMS	23.03	2.70
2-NBT-BT/PDMS	22.50	3.71
3-NBT-BT/PDMS	21.22	6.23
4-NBT-BT/PDMS	21.04	5.08
5-NBT-BT/PDMS	21.34	4.05

for the 3-NBT-BT/PDMS-based TENG, and then decreases, while the resistance at which the maximum occurs remains nearly constant for all compositions. The highest P_{max} value of 6.23 μW/cm^2 was recorded for the 3-NBT-BT/PDMS-based TENG at a R_{max} of 21.22 $M\Omega$, which is approximately five times greater than that of the pure PDMS-based device (1.28 μW/cm^2). These results suggest that, to maximize the energy harvesting performance from NBT-20BT/PDMS-based TENGs, the load resistance in the external circuit should be adjusted to ~ 20 $M\Omega$.

Furthermore, several key TENG performance characteristics were examined to assess device reliability and practical applicability. For this purpose, the 3-NBT-BT/PDMS-based TENG was selected. Stability and durability tests, as with all preceding triboelectric measurements, were performed under a "sawtooth"-profile contact–separation cycle, whereas frequency- and force-dependent I_{SC} signals were obtained using a symmetric "triangular"-profile contact–separation cycle. The output I_{SC} performance was analyzed as a function of frequency in the 1–4 Hz range at compressive force of 10 N (see Supporting Information, Figure S5(a)), and as a function of compressive force up to 30 N at frequency of 1 Hz (see Supporting Information, Figure S5(b)). Figure S5(a) shows that the I_{SC} is nearly independent of frequency within the studied range. In turn, increasing the applied compressive force results in a corresponding enhancement in the I_{SC} output signal (Figure S5(b)). Specifically, as the force increases from 5 to 30 N, the peak-to-peak I_{SC} value rises from 16.4 to 46.8 μ A. This trend is consistent with commonly reported observations in TENG studies, where output characteristics increase with applied compressive force [57,58]. A higher applied force increases the friction force, thereby enhancing triboelectric output. The I_{SC} results of the device stability and durability test over 15 k cycles, performed under a periodic compressive force of 10 N at a contact–separation frequency of 1 Hz, are provided in the Supporting Information (Figure S6(a)). Enlarged views of individual I_{SC} pulses at ~1 k-th and ~15 k-th cycles are shown in Figure S6(b,c), respectively. Notably, after ~15 k operating cycles, the 3-NBT-BT/PDMS-based TENG retains 98 % of its initial I_{SC} output. Moreover, the shape of the I_{SC} signal after 15 k cycles (see Fig. S6(c)) remains essentially unchanged compared to the initial signal (see Fig. S6(b)).

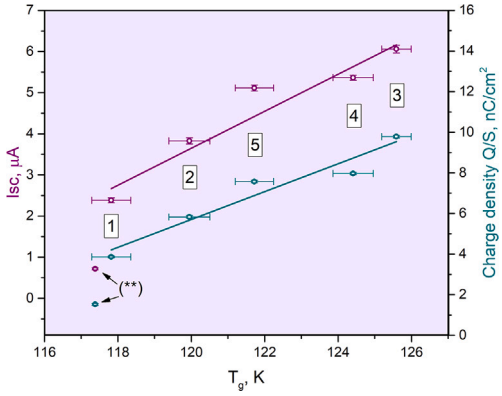

Fig. 10. Short-circuit current and surface charge density as a function of the glass transition temperature of NBT-20BT/PDMS composite films. The solid lines represent a linear fits. Here, (**) is T_g data for pure PDMS taken from ref. [32].

The behavior of both the glass transition temperature T_g and the output short-circuit current I_{sc} (or surface charge density Q/S) demonstrates a similar trend: all parameters reach a maximum for the 3-NBT-BT/PDMS sample. Scanning electron microscopy (see Fig. 3) shows that this sample contains agglomerated particles, in contrast to the 1-NBT-BT and 5-NBT-BT samples. The impact of agglomeration on the dielectric/triboelectric properties of the composites is more significant than the size of individual crystallites. In addition, another important tendency should be noted. Fig. 10 presents the mean peak I_{sc} and Q/S values as a function of the glass transition temperature T_g. It was previously demonstrated that the glass transition affects the performance of TENGs [59]. Usually, as the polymer gets harder, the charge decreases. A higher glass transition temperature means that the polymer chains have less mobility and a higher degree of ordering. In particular, it was shown that above the glass transition temperature, the response increases drastically compared to that below it [60,61]. Another factor that influences the charging is surface stickiness. Higher adhesion usually enhances the charge transfer. In addition, the additives may adsorb crosslinking initiator, thus reducing crosslinking degree, although in that case we would see a decrease in the glass transition temperature [28]. It can be proposed that the strong matrix-particle interaction provides inclusions with distinct mechanical properties from the surrounding rubbery matrix, which in turn, upon contact-separation, causes stress accumulation. Stress accumulation has been shown to improve and charge transfer [62]. The glass transition temperature is not directly related to the spatial distribution; however, it is related to grain size, which can limit or increase the mobility of polymer chains. This research shows that the distribution of filler at similar concentrations affects both T_g and triboelectric properties. As a result, even the glass transition temperature, which occurs well below room temperature (around 120 K), still correlates with the polymer's triboelectric properties at room temperature. However, the main physical reason behind the correlation is the different morphology of the filler; both the TENG performance and T_g share similar trends in their respective dependencies and are not directly dependent on one another. The dependencies I_{sc} (T_g) and Q/S(T_g) are nearly linear (see Fig. 10) for the composite films NBT-20BT/PDMS, while pure PDMS exhibits a lower response and does not fit the detected tendency.

4. Conclusions

A series of 14 vol.% NBT-20BT/PDMS-based triboelectric nanogenerators with different particle sizes were prepared using a

combination of simple dispersion and spin-coating methods. The NBT-20BT powder was synthesized via a conventional solid-state reaction method, and its particle size was subsequently reduced by applying wet planetary ball milling. The NBT-20BT/PDMS-based TENGs were investigated with respect to morphology, dielectric properties at various temperatures and frequencies, and triboelectric output performance.

Regarding the morphology, scanning electron microscopy was used to determine the NBT-20BT particle size and their distribution in PDMS. Statistical analysis of particle sizes obtained from SEM images demonstrated that they obey a Weibull distribution function. Moreover, the Weibull parameters, such as the scale parameter λ and the Weibull modulus k, decrease with increasing ball-milling time. This indicates that the particles are becoming finer (λ drops from 243 to 171 nm) and their size distribution is becoming narrower. The particle distribution in the PDMS matrix was homogeneous for all powders except 3-NBT-BT, which exhibited a significant number of agglomerates.

Loading PDMS with NBT-20BT particles significantly alters its dielectric properties. The dielectric permittivity of the NBT-20BT/PDMS composite films is higher than that of pure PDMS. At low temperatures, all samples exhibit a dynamic glass transition anomaly in the PDMS matrix, and their behavior depends on the NBT-20BT particle size. Specifically, the glass transition temperature T_g shifts to higher values than in pure PDMS due to the strong interaction between PDMS chains and NBT-20BT particles. This temperature shift (of about 9 K) occurs in a non-monotonic manner; namely, a maximum of T_g is observed for the 3-NBT-BT composite film.

The triboelectric output performance of the NBT-20BT/PDMS-based TENGs was tested against an Al foil in vertical contact-separation mode under pressing force of 10 N and at a frequency of 1 Hz. The addition of NBT-20BT particles into PDMS led to an increase in all triboelectric parameters, with the 3-NBT-BT/PDMS TENG exhibiting the highest values—6.06 μ A, 9.79 nC/cm^2, and 6.23 μW/cm^2 for the short-circuit current, charge density, and output power density (at R_{max} = 21.22 MΩ), respectively. Scanning electron microscopy explains the mentioned non-monotonic behavior through the pronounced agglomeration of the 3-NBT-BT powders in the PDMS matrix. Additionally, NBT-20BT/PDMS-based TENGs demonstrate remarkable device stability, maintaining 98 % of their initial I_{SC} output after ~15 k working cycles (tested for 3-NBT-BT/PDMS sample). An important correlation between the dielectric and triboelectric properties of NBT-20BT/PDMS composite films was detected: the TENG output performance depends on the glass transition temperature in a close to linear manner within the studied range.

CRediT authorship contribution statement

Žygimantas Logminas: Writing – review & editing, Writing – original draft, Validation, Investigation. **Darya Meisak:** Writing – review & editing, Writing – original draft, Methodology, Investigation, Conceptualization. **Līva Ģērmane:** Investigation. **Artyom Plyushch:** Writing – review & editing, Writing – original draft, Methodology, Investigation, Conceptualization. **Martynas Kinka:** Methodology, Investigation, Conceptualization. **Ugnius Sviackevičius:** Investigation. **Muhammad Shahzaib Asad:** Investigation. **Aleksej Zarkov:** Writing – review & editing, Investigation. **Gytis Sliaužys:** Investigation. **Rokas Dobužinskas:** Investigation. **Andris Šutka:** Writing – review & editing, Supervision. **Jūras Banys:** Supervision.

Funding

D.M. and M.K. extend their appreciation to the Research Council of Lithuania (LMTLT) for supporting this work under agreement No. S-LLT-26-3. The authors would also like to thank Victoria Kravchenko for her valuable discussions.

Declaration of competing interest

The authors declare that they have no known competing financial interests or personal relationships that could have appeared to influence the work reported in this paper.

Appendix A. Supplementary data

Supplementary data to this article can be found online at doi:10.1016/j.mtcomm.2026.115456.

Data availability

Data will be made available on request.

References

[1] A. Šutka, L. Lapčinskis, D. He, H. Kim, J.D. Berry, J. Bai, M. Knite, A.V. Ellis, C.K. Jeong, P.C. Sherrell, Engineering polymer interfaces: a review toward controlling triboelectric surface charge, Adv. Mater. Interfaces 10 (26) (2023) 2300323.
[2] F.-R. Fan, Z.-Q. Tian, Z.L. Wang, Flexible triboelectric generator, Nano Energy 1 (2) (2012) 328–334.
[3] G. Cheng, Z.-H. Lin, Z.-L. Du, Z.L. Wang, Simultaneously harvesting electrostatic and mechanical energies from flowing water by a hybridized triboelectric nanogenerator, ACS Nano 8 (2) (2014) 1932–1939.
[4] A.P.S. Prasanna, M. Anithkumar, S.-J. Kim, Hybrid triboelectric nanogenerators: revolutionizing the energy harvesting through material diversity and device architecture for different applications, Nano Energy 131 (2024) 110253.
[5] W. Peng, R. Zhu, Q. Ni, J. Zhao, X. Zhu, Q. Mei, C. Zhang, L. Liao, Functional tactile sensor based on arrayed triboelectric nanogenerators, Adv. Energy Mater. 14 (44) (2024) 2403289.
[6] P. Lu, X. Liao, X. Guo, C. Cai, Y. Liu, M. Chi, G. Du, Z. Wei, X. Meng, S. Nie, Gel-based triboelectric nanogenerators for flexible sensing: principles, properties, and applications, Nano-micro Lett. 16 (1) (2024) 206.
[7] H. Zhang, D. Zhang, Y. Yang, L. Zhou, Y. Liu, W. Liu, Y. Sun, Y. Guo, Y. Ji, Eco-friendly triboelectric nanogenerator for self-powering stacked In2O3 nanosheets/PPy nanoparticles-based NO_2 gas sensor, Nano Energy 128 (2024) 109978.
[8] U. Khan, S.-W. Kim, Triboelectric nanogenerators for blue energy harvesting, ACS Nano 10 (7) (2016) 6429–6432.
[9] Z.L. Wang, T. Jiang, L. Xu, Toward the blue energy dream by triboelectric nanogenerator networks, Nano Energy 39 (2017) 9–23.
[10] L. Liu, T. Hu, X. Zhao, C. Lee, Recent progress in blue energy harvesting based on triboelectric nanogenerators, Nanoenergy Adv. 4 (2) (2024) 156–173.
[11] L. Li, R. Wang, Y. Fu, Z. Jin, J. Chen, H. Du, X. Pan, Y.-C. Wang, Fabricating and engineering woody-biomass aerogels for high-performance triboelectric nanogenerators for energy harvesting and biomechanical monitoring, Adv. Funct. Mater. 35 (2) (2025) 2412324.
[12] Z. Zheng, X. Ma, M. Lu, H. Yin, L. Jiang, Y. Guo, High-performance all-textile triboelectric nanogenerator toward intelligent sports sensing and biomechanical energy harvesting, ACS Appl. Mater. Interfaces 16 (8) (2024) 10746–10755.
[13] H. Zou, L. Guo, H. Xue, Y. Zhang, X. Shen, X. Liu, P. Wang, X. He, G. Dai, P. Jiang, et al., Quantifying and understanding the triboelectric series of inorganic non-metallic materials, Nat. Commun. 11 (1) (2020) 2093.
[14] L. Lapčinskis, A. Linarts, K. Mālnieks, H. Kim, K. Rubenis, K. Pudzs, K. Smits, A. Kovaļovs, K. Kalniņš, A. Tamm, et al., Triboelectrification of nanocomposites using identical polymer matrixes with different concentrations of nanoparticle fillers, J. Mater. Chem. A 9 (14) (2021) 8984–8990.
[15] D. Anand, A.S. Sambyal, R. Vaid, A critical review on the material aspects of triboelectric nanogenerators (TENG), Facta Univ. Ser. Electron. Energ. 36 (3) (2023) 411–426.
[16] N. Buatip, D. Munthala, P. Amonpattaratkit, P. Pakawanit, X. Hu, W. Jongpinit, P. Janphuang, C. Wan, C. Bowen, S. Pojprapai, Piezo-tribo-electric nanogenerator based on BCZT/MCNTs/PDMS piezoelectric composite for compressive energy harvesting, Mater. Res. Bull. 173 (2024) 112686.
[17] W. Sun, Y. Wang, X. Lv, J. Dong, Y. Zhang, B. Chen, N. He, J. Liu, D. Nan, High-performance triboelectric nanogenerator with aminated barium titanate composite nanoparticles for early Parkinson's disease diagnosis, Chem. Eng. J. 500 (2024) 156710.
[18] H. Li, Y. Zhang, M. Yan, Y. Liu, M. Jia, S. Xiang, H. Gong, Q. Xu, X. Yuan, K. Zhou, et al., High-performance triboelectric nanogenerator based on high-permittivity BaZr0. 2Ti0. 8O3 nanowires with enhanced surface potential, Ceram. Int. 51 (9) (2025) 11211–11219.
[19] R. Umapathi, M. Rethinasabapathy, V. Kakani, H. Kim, Y. Park, H.K. Kim, G.M. Rani, H. Kim, Y.S. Huh, Hexagonal boron nitride composite film based triboelectric nanogenerator for energy harvesting and machine learning assisted handwriting recognition, Nano Energy 136 (2025) 110689.
[20] N. Madathil, A. Babu, M. Velupula, A. Kulandaivel, R.K. Rajaboina, U.K. Khanapuram, K.C. Devarayapalli, D.S. Lee, A layered double hydroxides/MXene composite based triboelectric nanogenerator for energy harvesting and self-powered electroplating applications, Sustain. Energy Fuels 9 (16) (2025) 4364–4374.

[21] P. Manchi, S.A. Graham, M.V. Paranjape, A. Kurakula, V.S. Kavarthapu, J.S. Yu, Calcium copper titanate incorporated polydimethylsiloxane flexible composite film-based triboelectric nanogenerator for energy harvesting and self-powered sensing applications, J. Mater. Sci. Technol. 190 (2024) 56–66.
[22] H.M. Venkatesan, I. Woo, J.U. Yoon, P. Gajula, A.P. Arun, J.W. Bae, Unveiling the latent potential: Ni/CoFe2O4-loaded electrospun PVDF hybrid composite-based triboelectric nanogenerator for mechanical energy harvesting applications, Adv. Compos. Hybrid Mater. 8 (2) (2025) 221.
[23] Y. Yang, X. Liang, L. Ma, M. Chen, L. Wu, Enhanced liquid–solid triboelectric nanogenerators with sio_2@ cu-doped composite coating for droplet energy harvesting, ACS Appl. Mater. Interfaces 17 (2025).
[24] A. Šutka, L. Lapčinskis, O. Verners, L. Ģērmane, K. Smits, A. Pludons, S. Gaidukovs, I. Jerāne, M. Zubkins, K. Pudzs, et al., Bio-inspired macromolecular ordering of elastomers for enhanced contact electrification and triboelectric energy harvesting, Adv. Mater. Technol. 7 (10) (2022) 2200162.
[25] S.S. Sundari, B. Kumar, R. Dhanasekaran, Synthesis, dielectric and relaxation behavior of lead free NBT–BT ceramics, Ceram. Int. 39 (1) (2013) 555–561.
[26] Š. Svirskas, T. Kudrevičius, E. Birks, M. Dunce, A. Sternbergs, C.-H. Huang, J. Banys, Dielectric and piezoelectric properties of 0.8 Na0. 5Bi0. 5TiO3-0.2 BaTiO3 modified with sodium niobate, Lith. J. Phys. 62 (4) (2022).
[27] Š. Svirskas, M. Dunce, E. Birks, A. Sternberg, J. Banys, Electromechanical properties of Na0. 5Bi0. 5TiO3-SrTiO3-PbTiO3 solid solutions, J. Phys. Chem. Solids 114 (2018) 94–99.
[28] A. Šutka, K. Mālnieks, L. Lapčinskis, M. Timusk, K. Kalniņš, A. Kovaļovs, J. Bitenieks, M. Knite, D. Stevens, J. Grunlan, Contact electrification between identical polymers as the basis for triboelectric/flexoelectric materials, Phys. Chem. Chem. Phys. 22 (23) (2020) 13299–13305.
[29] X. Meng, Z. Zhang, D. Lin, W. Liu, S. Zhou, S. Ge, Y. Su, C. Peng, L. Zhang, Effects of particle size of dielectric fillers on the output performance of piezoelectric and triboelectric nanogenerators, J. Adv. Ceram. 10 (5) (2021) 991–1000.
[30] M. Dunce, E. Birks, M. Antonova, A. Plaude, R. Ignatans, A. Sternberg, Structure and dielectric properties of Na1/2Bi1/2TiO3-BaTiO3 solid solutions, Ferroelectrics 447 (1) (2013) 1–8.
[31] M. Jurjans, L. Bikse, E. Birks, Š. Svirskas, M. Antonova, M. Kundzins, A. Sternberg, Electromechanical properties in CaTiO3 modified Na0. 5Bi0. 5TiO3-BaTiO3 solid solutions above morphotropic phase boundary, AIP Adv. 12 (3) (2022).
[32] D. Meisak, A. Plyushch, M. Kinka, S. Balciunas, V. Kalendra, S. Schaefer, A. Zarkov, A. Selskis, J. Banys, V. Fierro, et al., Effect of particle size on the origin of electromechanical response in BaTiO3/PDMS nanogenerators, ACS Appl. Electron. Mater. 6 (10) (2024) 7464–7474.
[33] A. Vaitkus, A. Merkys, T. Sander, M. Quirós, P.A. Thiessen, E.E. Bolton, S. Gražulis, A workflow for deriving chemical entities from crystallographic data and its application to the crystallography open database, J. Cheminformatics 15 (1) (Dec 2023), https://doi.org/10.1186/s13321-023-00780-2
[34] M. Dunce, E. Birks, M. Antonova, L. Bikse, S. Dutkevica, O. Freimanis, M. Livins, L. Eglite, K. Smits, A. Sternberg, Influence of sintering temperature on microstructure of Na0. 5Bi0. 5TiO3 ceramics, J. Alloys Compd. 884 (2021) 160955.
[35] G. Jones, P. Thomas, Investigation of the structure and phase transitions in the novel A-site substituted distorted perovskite compound Na0. 5Bi0. 5TiO3, Struct. Sci. 58 (2) (2002) 168–178.
[36] E. Aksel, J.S. Forrester, J.L. Jones, P.A. Thomas, K. Page, M.R. Suchomel, Monoclinic crystal structure of polycrystalline Na0. 5Bi0. 5TiO3, Appl. Phys. Lett. 98 (15) (2011).
[37] Y. Zhang, G. Buscarnera, I. Einav, Grain size dependence of yielding in granular soils interpreted using fracture mechanics, breakage mechanics and weibull statistics, Géotechnique 66 (2) (2016) 149–160.
[38] L. Wu, W. Krijgsman, J. Liu, C. Li, R. Wang, W. Xiao, CFLab: a MATLAB GUI program for decomposing sediment grain size distribution using weibull functions, Sediment. Geol. 398 (2020) 105590.
[39] M.A. Delfrate, J. Lemaitre, V. Buscaglia, M. Leoni, P. Nanni, Slip casting of submicron BaTiO3 produced by low-temperature aqueous synthesis, J. Eur. Ceram. Soc. 16 (9) (1996) 975–984.
[40] Y. Liang, M. Ozawa, A. Krueger, A general procedure to functionalize agglomerating nanoparticles demonstrated on nanodiamond, ACS Nano 3 (8) (2009) 2288–2296.
[41] O. Boorman, I. Hosier, M. Praeger, R. Torah, A. Vaughan, T. Andritsch, S. Swingler, J. Topham, Barium titanate and the dielectric response of polystyrene-based composites, in: 2014 IEEE Conference on Electrical Insulation and Dielectric Phenomena (CEIDP), IEEE, 2014, pp. 707–710.
[42] M. Takahashi, M. Oya, M. Fuji, Transparent observation of particle dispersion in alumina slurry using in situ solidification, Adv. Powder Technol. 15 (1) (2004) 97–107.
[43] T. Ogi, R. Zulhijah, T. Iwaki, K. Okuyama, Recent progress in nanoparticle dispersion using bead mill, KONA Powder Part. J. 34 (2017) 3–23.
[44] S. Marković, M. Mitrić, G. Starčević, D. Uskoković, Ultrasonic de-agglomeration of barium titanate powder, Ultrason. Sonochemistry 15 (1) (2008) 16–20.
[45] A. Plyushch, J. Macutkevič, J. Banys, P. Kuzhir, N. Kalanda, A. Petrov, C. Silvestre, M.A. Uimin, A.Y. Yermakov, O. Shenderova, Carbon-coated nickel nanoparticles: effect on the magnetic and electric properties of composite materials, Coatings 8 (5) (2018) 165.
[46] P.A. Klonos, Crystallization, glass transition, and molecular dynamics in PDMS of low molecular weights: a calorimetric and dielectric study, Polymer 159 (2018) 169–180.
[47] P. Klonos, A. Kyritsis, L. Bokobza, V.M. Gun'ko, P. Pissis, Interfacial effects in PDMS/titania nanocomposites studied by thermal and dielectric techniques, Colloids Surf. a Physicochem. Eng. Asp. 519 (2017) 212–222.
[48] I. Sulym, P. Klonos, M. Borysenko, P. Pissis, V.M. Gun'ko, Dielectric and thermal studies of segmental dynamics in silica/PDMS and silica/titania/PDMS nanocomposites, J. Appl. Polym. Sci. 131 (23) (2014).
[49] A. Łapińska, N. Grochowska, J. Antonowicz, P. Michalski, K. Dydek, A. Dużyńska, A. Daniszewska, M. Ojrzyńska, K. Zeranska, M. Zdrojek, Influence of the filler distribution on PDMS-graphene based nanocomposites selected properties, Sci. Rep. 12 (1) (2022) 19038.
[50] S. Liu, T. Hua, X. Luo, N. Yi Lam, X.-M. Tao, L. Li, A novel approach to improving the quality of chitosan blended yarns using static theory, Text. Res. J. 85 (10) (2015) 1022–1034.
[51] H.-W. Park, N.D. Huynh, W. Kim, C. Lee, Y. Nam, S. Lee, K.-B. Chung, D. Choi, Electron blocking layer-based interfacial design for highly-enhanced triboelectric nanogenerators, Nano Energy 50 (2018) 9–15.
[52] W. Seung, H.-J. Yoon, T.Y. Kim, H. Ryu, J. Kim, J.-H. Lee, J.H. Lee, S. Kim, Y.K. Park, Y.J. Park, et al., Boosting power-generating performance of triboelectric nanogenerators via artificial control of ferroelectric polarization and dielectric properties, Adv. Energy Mater. 7 (2) (2017) 1600988.
[53] W. Dong, M. Li, C. Chen, K. Xie, J. Hong, L. Yang, Flexible hybrid self-powered piezo-triboelectric nanogenerator based on BTO-PVDF/PDMS nanocomposites for human machine interaction, Sci. Rep. 15 (1) (2025) 15991.
[54] L. Ģērmane, L. Lapčinskis, M. Iesalnieks, A. Šutka, Surface engineering of PDMS for improved triboelectrification, Mater. Adv. 4 (3) (2023) 875–880.
[55] Z.L. Wang, Triboelectric nanogenerators as new energy technology for self-powered systems and as active mechanical and chemical sensors, ACS Nano 7 (11) (2013) 9533–9557.
[56] M.V. Paranjape, J. Kim, Y. Kim, E. Jo, S.A. Graham, P. Manchi, J.K. Lee, J.S. Yu, Perovskite V–NaNbO3 embedded PDMS composite film-based robust hybrid nanogenerator for efficient mechanical energy harvesting, Compos. Sci. Technol. 242 (2023) 110195.
[57] J. Shin, S. Ji, H. Cho, J. Park, Highly flexible triboelectric nanogenerator using porous carbon nanotube composites, Polymers 15 (5) (2023) 1135.
[58] M.-L. Seol, J.-W. Han, D.-I. Moon, M. Meyyappan, Hysteretic behavior of contact force response in triboelectric nanogenerator, Nano Energy 32 (2017) 408–413.
[59] W.-G. Kim, I.-W. Tcho, D. Kim, S.-B. Jeon, S.-J. Park, M.-L. Seol, Y.-K. Choi, Performance-enhanced triboelectric nanogenerator using the glass transition of polystyrene, Nano Energy 27 (2016) 306–312.
[60] A. Šutka, A. Linarts, K. Mālnieks, K. Stiprais, L. Lapčinskis, Dramatic increase in polymer triboelectrification by transition from a glassy to rubbery state, Mater. Horiz. 7 (2) (2020) 520–523.
[61] A. Sohn, J.H. Lee, H.-J. Yoon, H.H. Lee, S.-W. Kim, Self-boosted power generation of triboelectric nanogenerator with glass transition by friction heat, Nano Energy 74 (2020) 104840.
[62] M. Sow, R. Widenor, A. Kumar, S.W. Lee, D.J. Lacks, R.M. Sankaran, Strain-induced reversal of charge transfer in contact electrification, Angew. Chem. Int. Ed. 51 (11) (2012) 2695–2697.